DEVELOPPEMENT D'UNE NOUVELLE METHODE POUR L'EVALUATION DE LA TENUE A LA MER D'UN NAVIRE ANIME D'UNE VITESSE D'AVANCE DANS LA HOULE

Xiaobo CHEN[(1)*], **Youngmyung CHOI**[(1,2)], **Sime MALENICA**[(1)] and **Quentin DERBANNE**[(1)]

[(1)]Research Department, Bureau Veritas, Paris, France
[(2)]Dept. Naval Architecture and Ocean Engineering, PNU, Busan, Republic of Korea
[*]xiao-bo.chen@bureauveritas.com

SOMMAIRE

En choisissant le courant dévié par un navire (l'écoulement de double modèle) comme l'écoulement de base sur lequel est superposé l'écoulement de perturbation contenant une composante stationnaire et une instationnaire, une nouvelle linéarisation cohérente de l'écoulement de perturbation, en particulier, une nouvelle condition aux limites sur la surface libre, est formulée. Un nouveau système d'équations intégrales sur les frontières a été établi en appliquant le théorème de Green. Les équations intégrales comprennent une intégrale localisée sur une zone de surface libre proche du corps, sans l'intégrale le long de la ligne de flottaison qui est présente dans l'approche classique avec la linéarisation sur l'écoulement uniforme. Pour mieux représenter la physique, la fonction de Green est reformulée en tenant compte de la viscosité du fluide de sorte que les comportements singuliers et hautement oscillatoires disparaissent naturellement. L'intégration de la fonction Green sur les facettes planes est effectuée de manière précise en utilisant les nouvelles formulations analytiques. En plus d'imposer la nullité du potentiel sur la surface de flottaison à l'intérieur de la carène, une nouvelle base de solution du problème est ainsi établie. Des résultats numériques en très bon accord avec des mesures expérimentales montrent que la présente méthode fournit bien un outil fiable et pratique pour étudier les efforts sur un navire animé d'une vitesse d'avance dans la houle ainsi que les réponses du navire.

SUMMARY

By choosing the ship-shaped stream (double-body flow) as the base flow over which is superposed the perturbation flow containing steady and unsteady components, a consistent linearisation of perturbation flows, in particular, a new boundary condition on the free surface, is formulated. A new set of boundary integral equations (BIE) are established by applying the Green's theorem. The resultant BIE includes a localized free-surface integral in the vicinity of ship but without the troublesome waterline integral present in the classical Neumann-Kelvin approach (NK). The Green function associated with a pulsating and translating source is reformulated by considering the viscous effect so that the complex singular and highly-oscillatory behaviour disappear naturally. The integration of Green's function over flat panels is evaluated accurately by applying new analytical formulations. With extra integral equations imposed over the waterplane inside the ship hull to ensure the zero potential outside the fluid domain, a new sound base of solution for ship seakeeping with forward speed is thus established. Numerical results in good agreement with experimental measurements shows that this new method provides a reliable and practical method to evaluate wave loads and induced ship motions.

1. INTRODUCTION

Being critically important in the design of ships, many studies have been carried out in the past for studying ship seakeeping with forward speed. No need to mention the tremendous progress in applying CFD to ship seakeeping, we like to focus on the potential theory following the assumption of ideal fluid and irrotational flow, for the simple reason that a reliable and practical tool is needed in the daily activities of ship de-

sign to reply to many technical challenges timely.

Within the framework of potential theory, the governing equation in the fluid is in its simplest form - the Laplacian which guarantees the conservation of mass. Nevertheless, the boundary conditions are extremely complicated. In particular, that on the free surface contains quadratic and cubic products of the velocity potential combining both the kinematic requirement to ensure that a fluid particle on the free surface stays always on the surface, and the dynamic balance of pressures on the upper and lower sides including the difference equal to that due to surface tension if any. Furthermore, the complicated boundary condition is written on the surface whose position depends on the solution. To break this "uroboros" ring, the perturbation method is used. Indeed, the total flow can be written as the sum of a base one and perturbed one by assuming that the perturbation flow has an order of magnitude smaller than that of the base flow. By taking only all terms of leading order, a linearisation of the problem is then realized.

In the classical treatment of ship seakeeping problem, the uniform stream is chosen as the base flow over which the linearisation is referred to that of Neumann-Kelvin type. There have been two mainstream methods including one based on the use of free-surface Green's function (GFM) and another the Rankine source method (RSM). Being more advantageous than RSM, the classical GFM reduces the unknowns to those on the hull only since the Green's function satisfies the boundary condition on the free surface and the radiation condition which cause substantial difficulties in RSM. Furthermore, wavy properties (dispersive propagating waves) of potential flows are well represented by the Fourier elements in GFM while the Rankine source is fundamentally representative for local and non-wavy flows. One of the fair examples concerns the zero-speed case. The great success of GFM in practical applications shows that GFM is incomparably superior to RSM. Thus, many studies have been pursued in order to extend the success to the seakeeping with forward speed.

A non-exhaustive list of publications in the past Journées de l'Hydrodynamique includes the analysis on slender-ship approximations in [1] and [2] on the first two events, the studious work on the pulsating and translating Green's function in [3], [6] and [7], the theoretical developments in [5] and [11], the validations presented in [4], [8] and [9], the method based on the use of bi-quadratic patches in [10], and the development of multi-domain method (MDM) in [12] based on the subdivision of fluid domain by a control surface at a distance from the ship, and the use of GFM in the exterior domain from the control surface, and RSM in the interior domain between the ship hull and the control surface. This MDM has been extensively studied in [13]. However, the success has been limited since the critical elementary solutions like added-mass and damping coefficients are in good agreement with benchmark results only for very thin or slender ships. Results for a realistic or blunt ship were not convergent nor stable. The major difficulty has been identified as the accurate computation of Green's function, its derivatives and their integration on ship hull and, in particular, along the waterline, as well summarized in [14].

The analysis in [15] reveals the peculiar properties that Green's function is singular and highly oscillatory when a field point approaches to the track of the translating and pulsating source. Introduction of viscosity (and surface tension) presented in [16] is an activator to suppress troublesome short waves. Still the waterline is there. Numerical tests in [13] indicate well the linear system associated with the boundary integral equations is ill-conditioned due to the waterline integral. This waterline integral is derived in [17] for the first time by applying the Stokes' theorem to the integral representation on the free surface, wrongly omitted in many studies before.

To establish a sound theoretical base and develop a reliable numerical scheme, now it is essential to make a thorough analysis of the problem from a new point of view with different angles. Some important results of this analysis are presented here. For the sake of space, only a summary of main points is given in each section. First, a consistent linearisation of unsteady flow over the ship-shaped stream, often called double-body flow, yield a complex boundary condition on the free surface, presented in Section 2. The free-surface Green's function with the effect of viscosity and some of interesting features are presented in section 3. The new formulations to analytically integrate Green's function over flat panels are given afterwards. The boundary integral equations are summarized in Section 4 where we find our recompense that the complex boundary condition on the free surface leads to the disappearance of the waterline integral. The remaining free-surface integral is very local as

the integrand is only significant in the vicinity of ship. In Section 5, the hydrodynamic pressures and loads are given with some different decompositions. In particular, a speed-effect restoring force associated with the steady flow is expressed explicitly and included in the formulation of hydrodynamic coefficients. The numerical implementation is presented in Section 6 with numerical results including added-mass and damping coefficients, the wave exciting loads and induced ship motions. Finally, some discussion and conclusions are recited in Section 7.

2. UNSTEADY FLOWS

We define a Cartesian coordinate system translating at the speed U with the ship in the positive x-direction. The z-axis is positive upwards with the origin at the undisturbed free surface. Relative to this reference frame, there exists an ambient flow $-U\vec{i}$ opposite to ship forward direction. The deepwater case is considered throughout the paper.

2.1. General equations

The presence of ship in this ambient flow creates a ship-shaped steady flow around the hull, called base flow $\mathbf{W} = U\nabla(\bar{\phi} - x)$. In addition to this base flow, there should be a wavy steady flow $\nabla\phi$. When the ship oscillates about the reference frame or/and in incoming waves, there exist also unsteady flow $\nabla\psi$. The wavy steady and unsteady flows are called perturbation flow and represented by the velocity potential $\Phi = \phi + \psi$. All velocity potentials $(\bar{\phi}, \phi, \psi)$ satisfy the Laplace equation in the fluid. The total flow $\mathbf{W} + \nabla\Phi$ satisfies the kinematic and dynamic conditions written in the combined form

$$\begin{aligned} &\Phi_{tt} + g\Phi_z + 2\mathbf{W}\cdot\nabla\Phi_t \\ &+\mathbf{W}\cdot\nabla(\mathbf{W}\cdot\nabla\Phi) + \nabla\Phi\cdot(\mathbf{W}\cdot\nabla)\mathbf{W} \\ &= -2\nabla\Phi\cdot\nabla\Phi_t - (\mathbf{W}+\nabla\Phi)\cdot(\nabla\Phi\cdot\nabla)\Phi \\ &\quad -\nabla(\mathbf{W}\cdot\nabla\Phi)\cdot\nabla\Phi \\ &\quad -gU\bar{\phi}_z - \mathbf{W}\cdot(\mathbf{W}\cdot\nabla)\mathbf{W} \end{aligned} \tag{1}$$

on the free surface $z = \eta$ which is defined by

$$\begin{aligned} \eta = -\frac{1}{g}\Big[&(\partial_t + \mathbf{W}\cdot\nabla)\Phi + \frac{1}{2}\nabla\Phi\cdot\nabla\Phi \\ &+\frac{1}{2}(\mathbf{W}\cdot\mathbf{W} - U^2)\Big] \end{aligned} \tag{2}$$

The above equations (1) for potentials $\Phi = \phi+\psi$ and (2) for wave elevations are fully nonlinear with quadratic and cubic products of potentials and the assumption of time independence concerns only the base flow $\mathbf{W}$. Direct solutions of such problems with accuracy are extremely difficult if not impossible.

2.2. Linearisation on ship-shaped stream

We assume now the base flow $\mathbf{W} = U\nabla(\bar{\phi} - x)$ is of order $O(1)$ while the perturbation flows $\Phi = \phi + \psi$ are of smaller order $o(1)$ comparing to the base flow $(\bar{\phi} - x)$. In this way, the quadratic and cubic products of (ϕ, ψ) are ignored. Furthermore, the free-surface elevation η is also assumed to be of smaller order $o(1)$ which is true for small or moderate speed. The Taylor expansion of all terms in (1) with respect to $z = 0$ can be obtained by using

$$T|_{z=\eta} \approx T|_{z=0} + \eta T_z|_{z=0} \tag{3}$$

in which T represents any term in (1) and (2). Finally, the frequency-domain expression of unsteady potential is written as

$$\psi = \Re\mathrm{e}\{\varphi\,\mathrm{e}^{-\mathrm{i}\omega_e t}\}L\sqrt{gL} \tag{4}$$

with ω_e the encounter frequency, and the base flow $\mathbf{W} = U\mathbf{w}$ with $\mathbf{w} = \nabla\bar{\phi} - \vec{i}$ is used to obtain the linear boundary condition

$$\begin{aligned} &\varphi_z - \omega^2\varphi - 2\mathrm{i}\tau\mathbf{w}\cdot\nabla\varphi \\ &+F_\mathrm{r}^2\mathbf{w}\cdot\nabla(\mathbf{w}\cdot\nabla\varphi) + F_\mathrm{r}^2\nabla\varphi\cdot(\mathbf{w}\cdot\nabla)\mathbf{w} \\ &\quad +\bar{\phi}_{zz}(\mathrm{i}\tau\varphi - F_\mathrm{r}^2\mathbf{w}\cdot\nabla\varphi) = 0 \end{aligned} \tag{5}$$

on F i.e. $z = 0$. In (5), we have used the notations $\omega = \omega_e\sqrt{L/g}$ for dimensionless encounter frequency, $F_\mathrm{r} = U/\sqrt{gL}$ the Froude number and $\tau = \omega F_r$ the Brard number with L the ship length. Without considering the presence of ship, the classical Neumann-Kelvin linearisation is well based on uniform stream, i.e., taking $\bar{\phi} = 0$ and (5) becomes

$$\varphi_z - \omega^2\varphi + 2\mathrm{i}\tau\varphi_x + F_\mathrm{r}^2\varphi_{xx} = 0 \tag{6}$$

which is largely used in previous studies. The Neumann-Kelvin boundary condition (6) can be illustrated as the uniform stream penetrating in and through the ship hull (physically unacceptable) as shown by the left part of Figure 1. The linearisation based on the ship-shaped stream (5) is illustrated on the right part of Figure 1 which is physically acceptable.

The boundary condition on the ship hull is written on H at its mean position

$$\varphi_n = \begin{cases} -a\varphi_n^I & \text{diffraction} \\ -\mathrm{i}\omega\xi_j n_j + F_\mathrm{r}\xi_j m_j & \text{radiations} \end{cases} \tag{7}$$

The potential φ^I representing incoming waves is

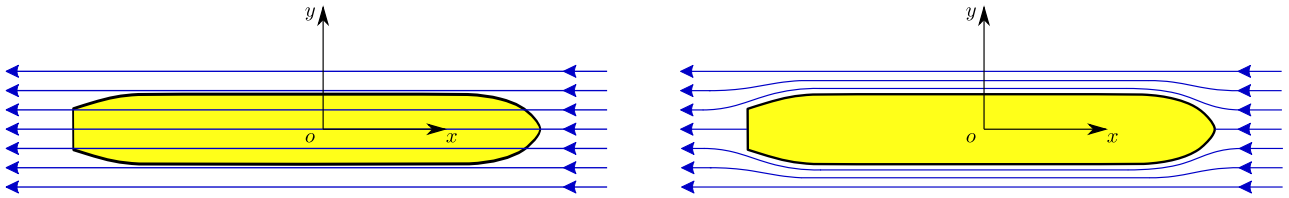

Figure 1. Uniform stream (left) *vs* ship-shaped stream (right) as the base flow in the linearisation

known to take Airy's form

$$\varphi^I = -\omega_0^{-1} \mathrm{e}^{k_0 z + \mathrm{i} k_0 (x\cos\beta + y \sin\beta)} \tag{8}$$

with the wave frequency ω_0 scaled with $\sqrt{L/g}$, the wavenumber $k_0 = \omega_0^2$ and wave heading β. The six elementary motions are denoted by ξ_j for $j = 1, 2, \cdots, 6$ including the translations $\mathbf{T} = (\xi_1, \xi_2, \xi_3)$ and rotations $\mathbf{R} = (\xi_4, \xi_5, \xi_6)$. The vector components (n_j, m_j) for $j = 1, 2, \cdots, 6$ are those of the generalized normal vector and those of m_j terms depending on ship-shaped stream $\mathbf{w}$ and explicitly given in [18]. It worth noting that the boundary condition (5) should be satisfied by the sum $\varphi^D + \varphi^I$ of diffraction potential φ^D and that of incoming waves φ^I so that (5) becomes non-homogenous (a non-zero forcing term) associated with φ^I for diffraction problem.

3. VISCOUS GREEN'S FUNCTION

We define the fundamental solution at the field point $P(\xi, \eta, \zeta)$ associated with a translating and pulsating source located at $Q(x, y, z)$, i.e. Green's function $G(P, Q)$ which satisfies the special equation of Poisson type

$$\nabla^2 G(P, Q) = 4\pi\delta(|P - Q|) \tag{9}$$

with $\delta(\cdot)$ the Dirac delta function, in the fluid domain. Based on the formal analysis of the Laplace-Fourier transform applied to the Stokes flow, in [16], the leading effect of vorticity is represented by an additional term appearing in the boundary condition at the free surface. Indeed, the linear boundary condition with dissipation is written by

$$\begin{aligned} G_z - \omega^2 G - 2\mathrm{i}\tau G_x + F_\mathrm{r}^2 G_{xx} \\ - 4\epsilon(F_\mathrm{r} G_{xxz} + \mathrm{i}\omega G_{zz}) = 0 \end{aligned} \tag{10}$$

on $z = 0$. In (10), the coefficient $\epsilon = \nu/\sqrt{gL^3}$ is proportional to the fluid kinematic viscosity ν. It is shown that the magnitude of elementary waves $\mathrm{e}^{k\zeta + \mathrm{i}(k\xi - \omega t)}$ decays like $\mathrm{e}^{-4\epsilon\omega k^2 |\xi|}$ and more rapidly with short waves of large wavenumber. This implies that the complex singular and highly oscillatory behaviours in $G(P, Q)$ due to short waves predicted in [15] just disappear.

By applying Fourier transform to differential equations satisfied by Green's function, we can express it by the sum of

$$4\pi G(P, Q) = -1/r + 1/r' + G^F(P, Q) \tag{11}$$

in which r is the distance between the source point $Q(x, y, z)$ and the field point $P(\xi, \eta, \zeta)$ and r' is that between the mirror source $Q'(x, y, -z)$ and $P(\xi, \eta, \zeta)$. The free-surface term $G^F(P, Q)$ is given by the Fourier integral in polar (k, θ) coordinates

$$G^F(P, Q) = \frac{1}{\pi F_\mathrm{r}^2} \int_{-\pi}^{\pi} \mathrm{d}\theta \int_0^{\infty} \mathrm{d}k \, \frac{k \mathrm{e}^{k(\mathrm{v} - \mathrm{i}w)}}{D(k, \theta)} \tag{12}$$

with the speed-scaled Fourier variable k and

$$\begin{aligned} \mathrm{v} &= (\zeta + z)/F_\mathrm{r}^2 \leq 0 \\ w &= \cos\theta(\xi - x)/F_\mathrm{r}^2 + \sin\theta(\eta - y)/F_\mathrm{r}^2 \end{aligned} \tag{13}$$

in their speed-scaled form.

3.1. Dispersion wavenumbers

The denominator of the integrand function in (12) is the dispersion function resultant from the Fourier transform of the boundary condition (10) in [16] :

$$D(k, \theta) = (k\cos\theta - \tau)^2 - k - \mathrm{i}4\epsilon(k\cos\theta - \tau)k^2 \tag{14}$$

The coefficient ϵ in (14) is scaled now by

$$\epsilon = \nu/(F_\mathrm{r}^3\sqrt{gL^3}) = \nu g/U^3 \tag{15}$$

The real part of $D(k, \theta)$ given in (14) is exactly the same as the classical dispersion function without viscosity. The equation for the real part of $\Re\{D(k, \theta)\} = 0$ has two roots, namely, the inviscid wavenumbers

$$\begin{aligned} k^- &= \tau^2/(1/2 + \sqrt{1/4 + \tau\cos\theta})^2 \\ k^+ &= (1/2 + \sqrt{1/4 + \tau\cos\theta})^2/\cos^2\theta \end{aligned} \tag{16}$$

to which one has to add an artificial and infinitesimal imaginary part (equivalent to $\epsilon \to 0^+$) multiplying a sign function to satisfy radiation condition. The complex dispersion function (14) represents the exact viscous effect and the required radiation condition is intrinsically satisfied by Green's function.

As the complex dispersion function $D(k,\theta)$ is independent of the sign of θ so that we consider only the case $\theta \in (0,\pi)$. The cubic dispersion equation $D(k,\theta)=0$ gives three complex roots denoted by :

$$k_{1,2,3}(\theta) = \kappa_{1,2,3}(\theta) + \mathrm{i}\mu_{1,2,3}(\theta) \qquad (17)$$

which can be found by applying Cardano's formulae invented in 16th century.

The three complex wavenumbers (k_1,k_2,k_3) are illustrated on the left, in the middle and on the right of Figure 2, respectively. The real and imaginary parts are represented against the value $\cos\theta$, by solid lines and dashed lines with symbols, respectively. One value $\epsilon = 0.0001$ is chosen, three $\tau = 1/5$, $1/4$ and $1/2$ are used and the associated curves are painted in black, red and blue colors, respectively. The first wavenumber k_1 scaled by F_{r}^2 in (14) is re-scaled by dividing τ^2. The wavenumbers k_2 and the real part κ_3 of k_3 are re-scaled by multiplying $\cos^2\theta$ while the imaginary part μ_3 of k_3 by $\epsilon\cos^2\theta$.

The first wavenumber k_1 is of finite magnitude. Its real part κ_1 is very close to k^- and its imaginary part $\mu_1 > 0$ and small for $\tau \le 1/4$. For $\tau > 1/4$, $\mu_1 \approx \sqrt{-1/4-\tau\cos\theta}/\cos^2\theta$ for $\theta \ge \pi - \theta_c$ with $\theta_c = \arctan\sqrt{16\tau^2-1}$. The second wavenumber k_2 is very different by its imaginary part $|\mu_2| \propto 4\epsilon|\kappa_2|^{5/2}$ while κ_2 can be very large for $|\theta-\pi/2| = \theta_m > 0$ and falls down to zero at $\theta = \pi/2$, elsewhere κ_2 is close to k^+ for $\epsilon \ll 1$. The third wavenumber k_3 is new and has a negative real part $\kappa_3 < 0$ and an imaginary part of very large magnitude $|\mu_3| \propto O(1/\epsilon)$. Except for $\tau > 1/4$ and $\theta > \pi - \theta_c$, $\mu_2 \approx -\sqrt{-1/4-\tau\cos\theta}/\cos^2\theta \approx -\mu_1$, the imaginary part of each wavenumber at different values of τ has closed values - the difference in function of τ is of order $O(\epsilon)$, so that the curves of imaginary part are indistinguishable .

As shown on the left part of Figure 3, the real part $\kappa_{1,2}(\theta)$ is illustrated on the Fourier (α,β) plane by $(\alpha,\beta) = \kappa_{1,2}(\cos\theta,\sin\theta)$. At large k, the inviscid wavenumber curve k^+ or $\kappa_2(\epsilon = 0^+)$ approaches to a parabola. With viscosity, the wavenumber curves bend back to the axis $\alpha = 0$. At small or moderate (α,β), the wavenumbers (κ_2 and k^+) are identical for small ϵ. On the right part of Figure 3, the imaginary part $\mu_2(\theta)$ of the complex wavenumber $k_2(\theta)$ for $\theta < \pi/2$, is depicted for $\epsilon = 10^{-4}, 10^{-3}, 10^{-2}$ by the height above the Fourier (α,β) plane along the associated κ_2 curves. The magnitude of μ_2 increases rapidly with the wavenumber.

Other interesting features of complex wavenumbers are shown in Figure 4. On the left part, the special case for $\tau = 1/4$ for which the classical inviscid wavenumebrs $k^{\mp}$ cross at the point $(\alpha = -1/4, \beta = 0)$. Since $|\nabla D| = 0$ at this point, $G^F(P,Q)$ is known to be singular for $\tau = 1/4$. With viscosity, κ_1 and κ_2 do not touch each other anymore and go smoothly through the axis $\beta = 0$ (wavenumber curves are symmetrical with respect to the axis $\beta = 0$). Indeed, $|\nabla D| = -\mathrm{i}\epsilon 5/4$ and the singularity in Green's function disappears simply. On the right part of Figure 4, the wavenumber curves for $\tau = 1/2$ are illustrated. Again the inviscid wavenumbers $k^{\mp}$ touch at the point $(\alpha = -\tau, \beta = \tau\sqrt{16\tau^2-1})$ at which the wavenumber vector is tangent to the wavenumber curves. The integrand function of Green's function has a square root singularity at this tangent point which merely induces some numerical difficulties as Green's function itself is regular for any $\tau > 1/4$. The viscosity wavenumber curves go distinguishably in the vicinity of the tangent point that benefits to numerical computations.

3.2. Formulations of Havelock type

Once the three complex roots are found, the major part of integrand function in (12) can be developed as

$$\frac{k}{D(k,\theta)} = \frac{A_1}{k-k_1} + \frac{A_2}{k-k_2} + \frac{A_3}{k-k_3} \qquad (18)$$

with the amplitude function (A_1,A_2,A_3) independent of space variable (P,Q) and the integral variable k are associated with (k_1,k_2,k_3), respectively. The wavenumber integral defined by

$$K(\theta) = \int_0^\infty \frac{\mathrm{e}^{k(\mathrm{v}-\mathrm{i}w)}}{k-(\kappa+\mathrm{i}\mu)}\,\mathrm{d}k = \mathbf{Cex}(Z) \qquad (19)$$
$$+\mathrm{i}\pi\left[\mathrm{sgn}(\mu) + \mathrm{sgn}(\mu\mathrm{v}-\kappa w)\right] H(\kappa)\exp(Z)$$

is given in [19] with

$$\mathbf{Cex}(Z) = \mathrm{e}^Z E_1(Z)\,,\ Z = (\kappa+\mathrm{i}\mu)(\mathrm{v}-\mathrm{i}w) \qquad (20)$$

and (v,w) defined by (13) while (κ,μ) representing the (real, imaginary) parts of either k_1,k_2 or k_3. Furthermore, $\mathrm{sgn}(\cdot)$ is the sign function and $H(\cdot)$ the Heaviside function. Finally, $E_1(\cdot)$ is the exponential-integral function defined by (eq.5.1.1) in [20].

Using (18) in (12) and representing the inner integral by the wavenumber integral function (19), Green's function is expressed by the single

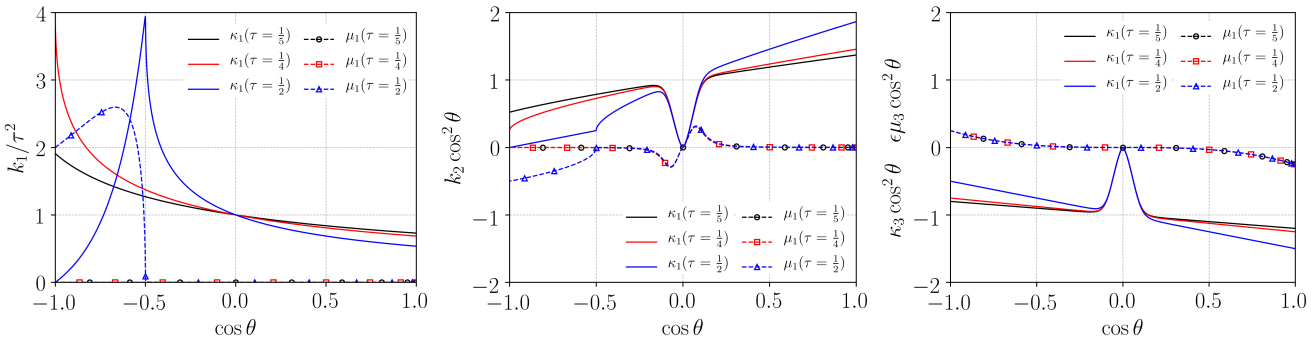

Figure 2. Complex wavenumbers for $\tau = 1/5$, $1/4$ and $1/2$ in function of $\cos\theta$: k_1/τ^2 (left), $k_2\cos^2\theta$ (middle) and $(\kappa_3, \epsilon\mu_3)\cos^2\theta$ (right)

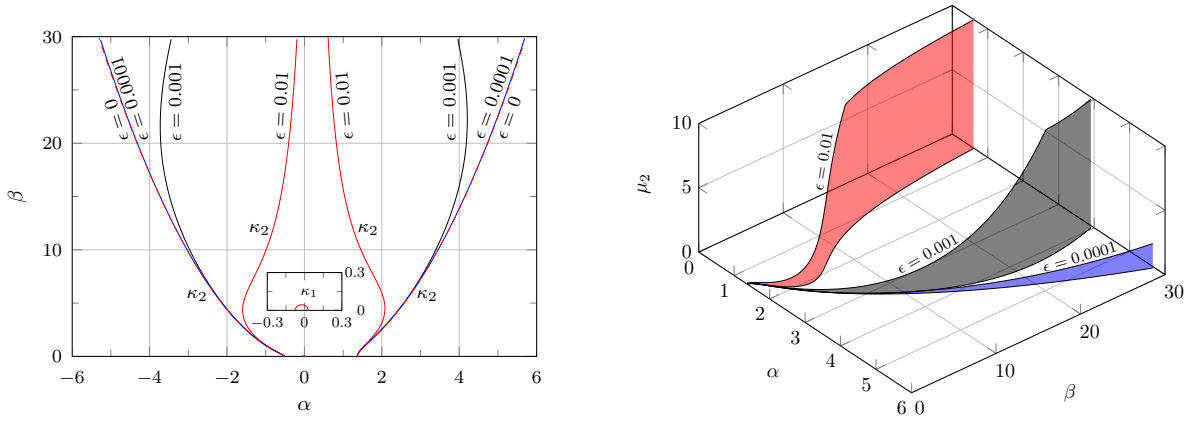

Figure 3. Wavenumber curves $k_{1,2}(\theta)$ at $\tau = 0.2$: (left) real part $\kappa_{1,2}(\theta)$ on the Fourier plane $(\alpha, \beta) = \kappa(\cos\theta, \sin\theta)$ and (right) its imaginary part $\mu_2(\theta)$ by the height above (α, β) plane.

θ-integral

$$G^F(P,Q) = \frac{1}{\pi F_r^2}\int_{-\pi}^{\pi}\Big[A_1K_1(\theta) + A_2K_2(\theta) + A_3K_3(\theta)\Big]\,\mathrm{d}\theta \tag{21}$$

of Havelock type. It worth noting that the amplitude function $A_j(\theta)$ for $j = 1, 2, 3$ in (21) are of regular function which can have sharp variation at $\theta = \pm(\pi - \theta_c)$ with $\theta_c = \arctan(16\tau^2 - 1)$ for $\tau > 1/4$. Furthermore, the wavenumber integral function $K(\theta) = K(P,Q) = K(a + ib)$ with (a, b) being real numbers depending on (κ, μ, v, w) according to its definition (19) is a regular function for $\mathrm{v} < 0$, except a logarithmic singularity at $\mathrm{v} = 0 = w$. Green's function represented by the single integral (21) can be then obtained by numerical integrations using trapeze or Gauss-Legendre algorithms.

The effect of viscosity is studied by illustrating the free-surface term $G^F(P,Q)$ defined by (21) in Figure 5. Its real (R.P.) and imaginary parts (I.P.) along a straight cut at $(x-\xi)/F_r^2 = -10$ on the free surface $\mathrm{v} = (z+\zeta)/F_r^2 = 0$ are depicted by red and blue solid lines, respectively, on the left. The pulsating and translating source is located at the origin for $\tau = 0.2$. The top part represents the values without viscosity ($\epsilon = 0^+$) while the bottom part depicts the values with viscosity ($\epsilon = 0.0001$). The singular and fast oscillations in the vicinity of source track (top) disappear with viscosity (bottom). On the right of Figure 5, the wave pattern is depicted with the real part and imaginary part on the up half and lower half, respectively.

3.3. Integrations of Green's function

In the case of the zero-speed problem, only one wavenumber exists for one frequency, i.e., oscillations of Green's function are associated with that wavenumber. Accurate integrations of Green's function can then be obtained by using one Gauss-point algorithm at panel's centroid if the panel size is enough small (one sixth) comparing to the wavelength. With forward speed, there is

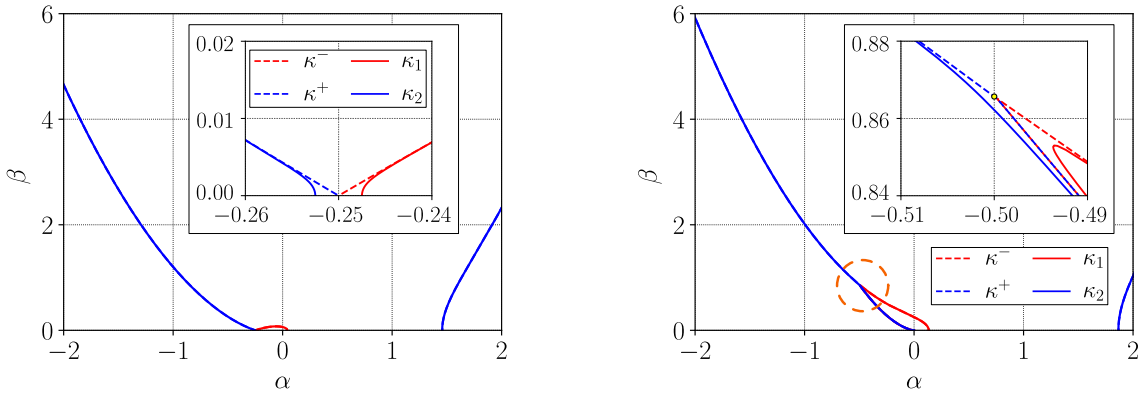

Figure 4. Wavenumbers $\kappa_{1,2}(\theta)$ on the Fourier plane $(\alpha,\beta)=\kappa(\cos\theta,\sin\theta)$ *vs* inviscid wavenumbers $k^{\mp}(\theta)$ for $\tau=1/4$ (left) and $\tau=1/2$ (right).

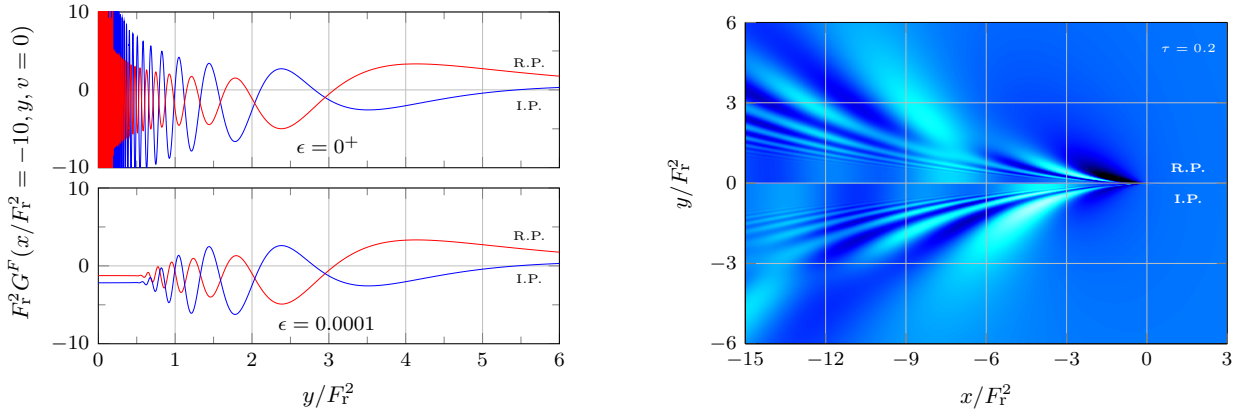

Figure 5. Green's function $G^F(P,Q)$ at $\tau=0.2$ along a strait cut (left) at $(x-\xi)/F_{\rm r}^2=-10$ and $\mathrm{v}=0=z+\zeta$ and its patterns (right) generated by a source at the free surface.

a large interval of wavenumbers from several finite values up to infinity. The introduction of viscosity gives some upper limits of wavenumbers from which higher oscillations are negligible. In order to obtain accurate integrations of Green's function associated with a limited interval of wavenumbers, the analytical integration over flat panels is considered. The flat panel h_q of polygon with m_q nodes is described by the node coordinates $Q_j(x_j,y_j,z_j)$ for $j=1,2,\cdots,m_q$ and connectivities from Q_j to Q_{j+1} with $Q_{m_q+1}=Q_1$ to close the contour. The normal vector is denoted as $\mathbf{n}^q=(n_1^q,n_2^q,n_3^q)$ according to the right-hand-thumb rule. The field point is denoted by $P(\xi,\eta,\zeta)$. The integration of the wavenumber integral function on the panel to the field point (P2C = panel to panel's centroid), shown on the left part of Figure 6, can be formulated as

$$C^q(P)=\iint_{h_q}K(P,Q)\,\mathrm{d}S(Q) \qquad (22)$$

$$=\frac{1}{k^2}\sum_{j=1}^{m_q}\Big\{\big[c_j^q+d_j^q k\big]\mathcal{K}(Z_j^P)+c_j^q R_1(Z_j^P)\Big\}$$

obtained in [19], inspired from the course handout [21], and by applying Stokes' theorem to transform an integral on panel surface to contour integrals along the panel's sides. In (22), $k=\kappa+\mathrm{i}\mu$ representing k_1, k_2 or k_3. Furthermore, the functions

$$\begin{aligned}\mathcal{K}(Z_j^P)&=K(kZ_j^P)+\ln(-Z_j^P)\\ R_1(Z_j^P)&=Z_j^P\big[\ln(-Z_j^P)-1\big]\end{aligned} \qquad (23)$$

are used with following notations

$$\begin{aligned}Z_j^P&=Z^P+Z_j\\ Z^P&=\zeta-\mathrm{i}(\xi\cos\theta+\eta\sin\theta)\\ Z_j&=z_j+\mathrm{i}(x_j\cos\theta+y_j\sin\theta)\end{aligned} \qquad (24)$$

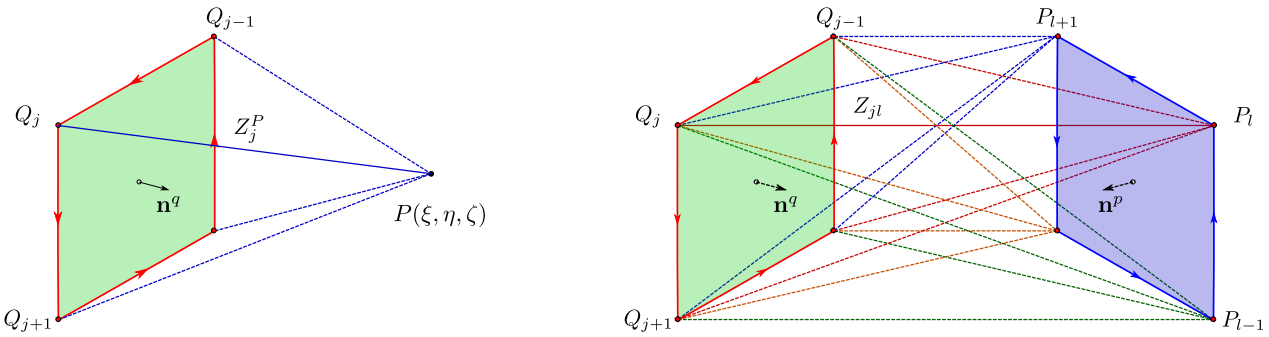

Figure 6. Integration of Green's function: scheme of P2C (left) and that of P2P (right)

The coefficients (c_j^q, d_j^q) in (22) are defined by

$$\begin{aligned}
c_j^q &= (n_2^q + \mathrm{i}n_3^q \sin\theta)\left[(x_j - x_{j-1})\delta_{j-1}^c \right. \\
&\qquad \left. - (x_{j+1} - x_j)\delta_j^c\right] \\
&\quad - (n_1^q + \mathrm{i}n_3^q \cos\theta)\left[(y_j - y_{j-1})\delta_{j-1}^c \right. \\
&\qquad \left. - (y_{j+1} - y_j)\delta_j^c\right] \\
d_j^q &= (n_2^q + \mathrm{i}n_3^q \sin\theta)\left[(x_j - x_{j-1})\delta_{j-1}^d \right. \\
&\qquad \left. + (x_{j+1} - x_j)\delta_j^d\right] \\
&\quad - (n_1^q + \mathrm{i}n_3^q \cos\theta)\left[(y_j - y_{j-1})\delta_{j-1}^d \right. \\
&\qquad \left. + (y_{j+1} - y_j)\delta_j^d\right]
\end{aligned} \tag{25}$$

$$\delta_j^c = \begin{cases} 1/(Z_{j+1} - Z_j) & |Z_{j+1} - Z_j| > 0 \\ 0 & |Z_{j+1} - Z_j| = 0 \end{cases}$$

$$\delta_j^d = \begin{cases} 0 & |Z_{j+1} - Z_j| > 0 \\ 1/2 & |Z_{j+1} - Z_j| = 0 \end{cases}$$

for $j = 1, 2, \cdots, m_q$ and noting that the subscript sequence $(\cdot)_0 = (\cdot)_{m_q}$ and $(\cdot)_{m_q+1} = (\cdot)_1$ in applying (25).

Furthermore, the second-fold integration on the panel h_p of polygon with m_p nodes denoted by $P_\ell(\xi_\ell, \eta_\ell, \zeta_\ell)$, as shown on the right part of Figure 6, has also been analysed in [19] with the same technique. This P2P (panel to panel) integration is written by

$$\begin{aligned}
C^{pq} &= \iint_{h_p} C^q(P)\,\mathrm{d}S(P) \\
&= \iint_{h_p}\Big[\iint_{h_q} K(P,Q)\,\mathrm{d}S(Q)\Big]\,\mathrm{d}S(P) \\
&= \frac{1}{k^4}\sum_{\ell=1}^{m_p}\sum_{j=1}^{m_q}\Big\{\big[c_j^q c_\ell^p + (c_j^q d_\ell^p + c_\ell^p d_j^q)k + d_j^q d_\ell^p k^2\big]\mathcal{K}(Z_{j\ell}) \\
&\quad + k\big[c_j^q c_\ell^p + (c_j^q d_\ell^p + c_\ell^p d_j^q)k + d_j^q d_\ell^p k^2\big]R_1(Z_{j\ell}) \\
&\quad + k^2\big[c_j^q c_\ell^p + (c_j^q d_\ell^p + c_\ell^p d_j^q)k\big]R_2(Z_{j\ell}) \\
&\quad + d_j^q d_\ell^p k^3 R_3(Z_{j\ell})\Big\}
\end{aligned} \tag{26}$$

with the additional notations

$$\begin{aligned}
R_1(Z_{j\ell}) &= Z_{j\ell}\big[\ln(-Z_{j\ell}) - 1\big] \\
R_2(Z_{j\ell}) &= Z_{j\ell}^2\big[2\ln(-Z_{j\ell}) - 3\big]/4 \\
R_3(Z_{j\ell}) &= Z_{j\ell}^3\big[6\ln(-Z_{j\ell}) - 11\big]/36 \\
Z_{j\ell} &= Z_j + Z_\ell
\end{aligned} \tag{27}$$

and coefficients (c_ℓ^p, d_ℓ^p) are formulated in the same way as (c_j^q, d_j^q) in (25) and involve the coordinates $P_\ell(\xi_\ell, \eta_\ell, \zeta_\ell)$, the normal vector $\mathbf{n}^p = (n_1^p, n_2^p, n_3^p)$, and Z_ℓ in place of $Q_j(x_j, y_j, z_j)$, $\mathbf{n}^q = (n_1^q, n_2^q, n_3^q)$, and Z_j, respectively.

From (25) and (27), the coefficients (Z_j, c_j^q, d_j^q) and $(Z_\ell, c_\ell^p, d_\ell^p)$ depend only on the geometry of panel h_q and h_p, respectively. The functions $\mathcal{K}(Z_j^P)$ and $\mathcal{K}(Z_{j\ell})$ has finite values for $Z_j^P \to 0$ and $Z_{j\ell} \to 0$, respectively. The same for auxiliary functions $R_{1,2,3}(Z)$ when $Z \to 0$. For large values of Z, alternative formulae are developed for $C^q(P)$ and C^{pq} well suit for their numerical evaluation. Concerning the logarithmic function appearing in $\mathcal{K}(Z)$ and $R_{1,2,3}(Z)$, theoretically, both $\ln(Z)$ and $\ln(-Z)$ are correct in the formulation. The logarithmic function $\ln(-Z)$ with negative sign is chosen in order to avoid the difficulty relative to the branch cut if $\ln(Z)$ is adopted, due to the fact that $\Re\mathrm{e}\{Z\} \le 0^-$ in all applications here.

Finally, the integrations of Green's function defined by (21) are then

$$\begin{aligned}
&F_\mathrm{r}^2 \iint_{h_q} G^F(P,Q)\,\mathrm{d}S(Q) \\
&= \frac{1}{\pi}\int_{-\pi}^{\pi}\big[A_1 C_1^q(\theta) + A_2 C_2^q(\theta) + A_3 C_3^q(\theta)\big]\,\mathrm{d}\theta \\
&F_\mathrm{r}^2 \iint_{h_p}\Big[\iint_{h_q} G^F(P,Q)\,\mathrm{d}S(Q)\Big]\,\mathrm{d}S(P) \\
&= \frac{1}{\pi}\int_{-\pi}^{\pi}\big[A_1 C_1^{pq}(\theta) + A_2 C_2^{pq}(\theta) + A_3 C_3^{pq}(\theta)\big]\,\mathrm{d}\theta
\end{aligned} \tag{28}$$

reduced to single θ-integrals which can be evaluated numerically. The formulations to perform the analytical integration of $\nabla G(P,Q)$ over panels are also developed in [19].

The coefficients d_j^q (and its pair d_ℓ^p) defined in (25) is nil except at two critical θ-values at which the wavenumber vector is orthogonal to the direction in parallel to the segment Q_j-to-Q_{j+1} of panel h_q when both Q_j and Q_{j+1} are located at the same level ($z_j = z_{j+1}$). However, ignoring d_j^q (or d_ℓ^p) can lead to significant numerical errors. Furthermore, the accuracy requirement for $K(Z)$ is more exigent in the numerical computation of P2P than P2C when θ is close to the critical values.

4. INTEGRAL EQUATIONS

There are three classical Green's theorems derived from the divergence theorem to make equality of the volume integral and the surface integrals over all boundaries, and the application to two harmonic functions. Especially, the third Green's theorem leads to the integral representation

$$C*\varphi(P)=\iint_{H\cup F\cup\Sigma}\big[\varphi_n(Q)G(P,Q)-\varphi(Q)G_n(P,Q)\big]\,\mathrm{d}S \tag{29}$$

resultant from the volume integral for the left hand side, and surface integrals over all $H\cup F\cup\Sigma$ including the ship hull H, the free surface F and a fictitious surface at infinity Σ on the right hand side. Besides the integral at infinity Σ which can be shown to disappear, different BIEs can be obtained following the boundary conditions, in particular, that on the free surface, and the consideration to preserve the well-conditioned system. The multiplicative constant $C = 1$ for any field point P in the domain, $C = 1/2$ for P on H and $C = 0$ for P outside of the domain. For a field point $P \in F$ on the free surface, more special analyses are needed. Indeed, a variant of Green's theorem (fourth one) is formulated in [19], by extending the analysis in [22] for the zero-speed case, and applied to obtain the constant $C = 1$ on the left hand side of integral representation (29) for a point $P \in F$ on the free surface.

4.1. Classical BIE on the ship hull

The boundary condition (6) on the free surface F in the classical Neumann-Kelvin method is based on the uniform stream. The F-integral on the right hand side of (29) can be reduced to an integral along the waterline

$$\begin{aligned} I_F &= \iint_F \big(-\varphi_z G+\varphi G_z\big)\,\mathrm{d}S \\ &= \oint_\Gamma \big[2\mathrm{i}\tau\varphi G + F_\mathrm{r}^2(\varphi_x G-\varphi G_x)\big]\,\mathrm{d}y \end{aligned} \tag{30}$$

by applying the Stokes' theorem, so that the classical BIE for $P \in H$ is written as

$$\begin{aligned} &\frac{1}{2}\varphi(P)+\iint_H \varphi G_n\,\mathrm{d}S \\ &+\oint_\Gamma\big[F_\mathrm{r}^2(\varphi G_x - c_t\varphi_t G - c_s\varphi_s G)-2\mathrm{i}\tau\varphi G\big]\,\mathrm{d}y \\ &\qquad = \iint_H \varphi_n G\,\mathrm{d}S + F_\mathrm{r}^2\oint_\Gamma c_n\varphi_n G\,\mathrm{d}y \end{aligned} \tag{31}$$

in which we have introduced the identity $\varphi_x = c_t\varphi_t + c_s\varphi_s + c_n\varphi_n$ with coefficients (c_t, c_s, c_n) depending on the hull geometry and $(\varphi_t, \varphi_s, \varphi_n)$ the two tangent derivatives and normal derivative along Γ.

4.2. New BIE on H, F and W

The boundary condition (5) on the free surface F based on the ship-shaped stream is now considered. Unlike the Neumann-Kelvin case, the analysis in [19] gives the F-integral

$$\begin{aligned} I_F &= \iint_F\Big[\bar\nabla\cdot(F_w\mathbf{w})+F_0\varphi+F_1\varphi_x+F_2\varphi_y\Big]\mathrm{d}S \\ &= -\oint_\Gamma F_w(\mathbf{w}\cdot\bar{\mathbf{n}})\,\mathrm{d}l+\iint_F(F_0\varphi+F_1\varphi_x+F_2\varphi_y)\,\mathrm{d}S \end{aligned} \tag{32}$$

with

$$\begin{aligned} F_w &= -2\mathrm{i}\tau\varphi G + F_\mathrm{r}^2\big[(\mathbf{w}\cdot\nabla\varphi)G-(\mathbf{w}\cdot\nabla G)\varphi\big] \\ F_0 &= 2\mathrm{i}\tau(\bar\phi_x G_x+\bar\phi_y G_y)-\mathrm{i}\tau\bar\phi_{zz}G \\ &\quad +F_\mathrm{r}^2[(\bar\phi_x-1)(2\bar\phi_{xx}+\bar\phi_{yy})+\bar\phi_y\bar\phi_{xy}]G_x \\ &\quad +F_\mathrm{r}^2[(\bar\phi_x-1)\bar\phi_{xy}+\bar\phi_y(\bar\phi_{xx}+2\bar\phi_{yy})]G_y \\ &\quad +F_\mathrm{r}^2[(\bar\phi_x-2)\bar\phi_x G_{xx}+2(\bar\phi_x-1)\bar\phi_y G_{xy}+\bar\phi_y^2 G_{yy}] \\ F_1 &= F_\mathrm{r}^2[(\bar\phi_x-1)\bar\phi_{xx}+\bar\phi_y\bar\phi_{xy}]G \\ F_2 &= F_\mathrm{r}^2[(\bar\phi_x-1)\bar\phi_{xy}+\bar\phi_y\bar\phi_{yy}]G \end{aligned}$$

The waterline integral on the right hand side of (32) is obtained by applying Gauss' theorem with notations $\bar\nabla = (\partial_x, \partial_y)$ and $\bar{\mathbf{n}} = (n_x, n_y)$. According to the boundary condition of ship-shaped stream on H and $\bar\phi_z = 0$ on F, the term $\mathbf{w}\cdot\bar{\mathbf{n}} \equiv 0$ along Γ. The waterline integral disappears simply. The remaining integral on F is significant only in the vicinity of H since the space derivatives of ship-shaped flow $\nabla\bar\phi$ and $\nabla(\nabla\bar\phi)$ decay rapidly away from the ship. It worths

noting that the first tentative to trait the same free-surface integral (32) was presented in [25] in which the terms with (F_1, F_2) are missing.

The new BIE on ship hull is then written as

$$\begin{aligned} \frac{1}{2} * \varphi(P) + \iint_H \varphi G_n \,\mathrm{d}S \\ -\iint_F (F_0\varphi + F_1\varphi_x + F_2\varphi_y)\,\mathrm{d}S = \iint_H \varphi_n G \,\mathrm{d}S \end{aligned} \tag{33}$$

for $P \in H$, which should be combined with one BIE on the free surface since $(\varphi, \varphi_x, \varphi_y)$ are unknown on F. Similar to the new BIE on H, the BIE for a field point P on the free surface is obtained

$$\begin{aligned} 1 * \varphi(P) + \iint_H \varphi G_n \,\mathrm{d}S \\ -\iint_F (F_0\varphi + F_1\varphi_x + F_2\varphi_y)\,\mathrm{d}S = \iint_H \varphi_n G \,\mathrm{d}S \end{aligned} \tag{34}$$

for $P \in F$. In addition, we apply the third Green's theorem (29) to a field point P located inside the ship, i.e., outside of the fluid domain limited by $H \cup F \cup \Sigma$. In particular, at some points on the waterplane denoted by W, the integral equation is written as

$$\begin{aligned} 0 * \varphi(P) + \iint_H \varphi G_n \,\mathrm{d}S \\ -\iint_F (F_0\varphi + F_1\varphi_x + F_2\varphi_y)\,\mathrm{d}S = \iint_H \varphi_n G \,\mathrm{d}S \end{aligned} \tag{35}$$

for $P \in W$ inside the ship hull.

As mentioned forgoing, there is, in addition, an integral on F on the right hand side of (33)-(35) associated with the forcing term due to incoming waves for diffraction problem, omitted here for the sake of space. The linear system combining BIE on H (33) and BIE on F (34) is of square form, i.e., the same number of equations as that of unknowns, since the tangent derivatives of unknowns on F can be transformed to unknowns φ by using shape functions in higher-order patch method, or any scheme of finite-difference type. In order to be sure that Green's theorem is well respected outside of the fluid domain - zero potential inside the ship. The additional equation (35) is formulated for $P \in W$ on the waterplane W. The system is then over-determined. The resolution of a linear system of rectangular form can be well obtained using the standard Lapack library.

5. WAVE LOADS AND MOTIONS

According to the boundary condition (7) on the ship hull H, the time-harmonic potential φ can be written as the sum $\varphi = a\varphi^D + \varphi^R$ of the diffraction φ^D and radiation φ^R decomposed by

$$\varphi^R = -\mathrm{i}\omega \sum_{j=1}^{6} \xi_j \varphi_j + F_\mathrm{r} \sum_{j=1}^{6} \xi_j \varphi_{j+6} \tag{36}$$

in which the first 12 elementary potentials are due to ship's motions ξ_j for $j = 1, 2, \cdots, 6$ including the translations $\mathbf{T} = (\xi_1, \xi_2, \xi_3)$ and rotations $\mathbf{R} = (\xi_4, \xi_5, \xi_6)$, called the radiation potential and satisfy the boundary condition on H

$$\frac{\partial}{\partial n}\varphi_j = \begin{cases} n_j & j = 1, 2, \cdots, 6 \\ m_{j-6} & j = 7, 8, \cdots, 12 \end{cases} \tag{37}$$

respectively. The diffraction potential φ^D associated with the wave amplitude a and the incoming waves φ^I given by (8) satisfies a non-homogeneous condition on F, as already mentioned. The new BIE (33)-(35) are directly applied to all φ_j for $j = 1, 2, \cdots, 12$ and φ^D for which an integral on F with the integrand function associated with the known φ^I on the right hand of new BIE (33)-(35).

5.1. Hydrodynamic pressures

Once we solve the new BIE and obtain φ_j for $j = 1, 2, \cdots, 12$, the time-harmonic pressure scaled with $(\rho g L)$ due to radiation can be obtained by Bernoulli's equation

$$\begin{aligned} P^R &= -\Big\{ -\mathrm{i}\omega\varphi^R + F_\mathrm{r}(\mathbf{w}\cdot\nabla)\varphi^R \Big\} \\ &= \sum_{j=1}^{6} \xi_j \Big\{ \omega^2\varphi_j + \mathrm{i}\tau\big[(\mathbf{w}\cdot\nabla)\varphi_j + \varphi_{j+6}\big] \\ &\qquad - F_\mathrm{r}^2(\mathbf{w}\cdot\nabla)\varphi_{j+6} \Big\} \end{aligned} \tag{38}$$

by introducing the radiation part in (36) and considering the notation for the time derivative of the time-harmonic potential $\psi_t = -\mathrm{i}\omega\varphi$. In the same way, the dynamic pressure due to diffraction scaled with $\rho g a$ is contributed by the sum of the incoming and diffraction potentials

$$P^D = \mathrm{i}\omega(\varphi^I + \varphi^D) - F_\mathrm{r}(\mathbf{w}\cdot\nabla)(\varphi^I + \varphi^D) \tag{39}$$

In addition, the hydrostatic pressure P^H and that P^S due to steady base flow are written by

$$\begin{aligned} \overline{P} &= P^H + F_\mathrm{r}^2 P^S \qquad \text{with} \\ P^H &= -z \\ P^S &= -\frac{1}{2}(\mathbf{w}\cdot\mathbf{w} - 1) \\ &= -\frac{1}{2}\big[(\bar\phi_x - 2)\bar\phi_x + \bar\phi_y\bar\phi_y + \bar\phi_z\bar\phi_z\big] \end{aligned} \tag{40}$$

which yield the usual hydrostatic stiffness due to the variation of P^H associated with the ship motion and the speed-effect restoring force due to the variation of P^S associated with the same ship motion. The second one is often ignored in the literature.

5.2. Radiation forces

The radiation forces are defined as the reaction of fluid via pressure on the ship hull against the displacement, velocity and acceleration of the ship, under the chosen reference system associated with the mean position of the ship. They are often written with a negative sign by

$$\begin{aligned} -F_i^R &= -\iint_H P^R N_i \,\mathrm{d}S \\ &\quad -\iint_H \big[(\boldsymbol{X}\cdot\nabla)\overline{P} + \overline{P}\boldsymbol{R}\wedge\big] N_i \,\mathrm{d}S \\ &= \sum_{j=1}^{6} \xi_j \big[-\omega^2 A_{ij} - \mathrm{i}\omega B_{ij} + C_{ij}\big] \end{aligned} \tag{41}$$

for $i = 1, 2, \cdots, 6$, in which A_{ij}, B_{ij} and C_{ij} are called added-mass, damping and stiffness coefficients, respectively, following their respective association with the acceleration, velocity and movement of the ship. The generalized normal vector $\boldsymbol{N} = (\boldsymbol{n}, \boldsymbol{r}\wedge\boldsymbol{n})^T = \{N_i\}$ is a column of 6 elements. Among all terms in (41), the simplest ones are associated with the hydrostatic pressure

$$-\iint_H \big[(\mathbf{X}\cdot\nabla)P^H + P^H\mathbf{R}\wedge\big] N_i \,\mathrm{d}S = \sum_{j=1}^{6} \xi_j H_{ij} \tag{42}$$

with the displacement vector

$$\begin{aligned} \boldsymbol{X} &= \boldsymbol{T} + \boldsymbol{R}\wedge\boldsymbol{r} \\ \boldsymbol{r} &= (x - x_0, y - y_0, z - z_0) \end{aligned} \tag{43}$$

associated with the translation/rotation $(\boldsymbol{T}, \boldsymbol{R})$ and the position vector $\boldsymbol{r}$ with respect to the reference point $\boldsymbol{r}_0 = (x_0, y_0, z_0)$. The hydrostatic stiffness matrix H_{ij} defined by (42) should be augmented by including the variation of gravity forces due to ship displacement, explained in all textbooks.

In the same way, the speed-effect stiffness coefficients are given by

$$-\iint_H \big[(\mathbf{X}\cdot\nabla)P^S + P^S\mathbf{R}\wedge\big] N_i \,\mathrm{d}S = \sum_{j=1}^{6} \xi_j S_{ij} \tag{44}$$

Concerning the radiation forces due to the time-harmonic pressure P^R defined by (38), we may decompose them into three components

$$-\iint_H P^R N_i \,\mathrm{d}S = \sum_{j=1}^{6} \xi_j \Big[-\omega^2 R_{ij}^{\omega} - \mathrm{i}\tau R_{ij}^{\tau} + F_{\mathrm{r}}^2 R_{ij}^{F_{\mathrm{r}}}\Big] \tag{45}$$

with

$$\begin{aligned} R_{ij}^{\omega} &= \iint_H \varphi_j N_i \,\mathrm{d}S \\ R_{ij}^{\tau} &= \iint_H \big[(\boldsymbol{w}\cdot\nabla)\varphi_j + \varphi_{j+6}\big] N_i \,\mathrm{d}S \\ R_{ij}^{F_{\mathrm{r}}} &= \iint_H (\boldsymbol{w}\cdot\nabla)\varphi_{j+6}\, N_i \,\mathrm{d}S \end{aligned} \tag{46}$$

By introducing (42), (44) and (45) back to (41) and following the usual notations, we have

$$\begin{aligned} A_{ij} &= \Re\mathrm{e}\Big\{ R_{ij}^{\omega} + \mathrm{i}(\tau/\omega) R_{ij}^{\tau} - (F_{\mathrm{r}}^2/\omega^2)\big[R_{ij}^{F_{\mathrm{r}}} + S_{ij}\big]\Big\} \\ B_{ij} &= \Im\mathrm{m}\Big\{ \omega R_{ij}^{\omega} + \mathrm{i}\tau R_{ij}^{\tau} - (F_{\mathrm{r}}^2/\omega) R_{ij}^{F_{\mathrm{r}}}\Big\} \\ C_{ij} &= H_{ij} \end{aligned} \tag{47}$$

in which the speed-effect stiffness S_{ij} (pure real) contributing to the added-mass coefficients, is fully ignored in all previous studies. A more consistent decomposition by regrouping terms associated with $R_{ij}^{F_{\mathrm{r}}}$ at the limit of zero frequency and S_{ij} in C_{ij} is suggested in [19].

5.3. Wave exciting forces and motions

The diffraction wave loads are often called the wave exciting loads and defined by the integration of time-harmonic diffraction pressure

$$\begin{aligned} F_i^D &= -\iint_H P^D N_i \,\mathrm{d}S \\ &= -\iint_H \Big\{ \mathrm{i}\omega(\varphi^I + \varphi^D) \\ &\qquad - F_{\mathrm{r}}(\mathbf{w}\cdot\nabla)(\varphi^I + \varphi^D)\Big\} N_i \,\mathrm{d}S \end{aligned} \tag{48}$$

which is proportional to the wave amplitude a. The motion equation based on the Newton's second law is expressed by

$$\sum_{j=1}^{6} \xi_j \Big\{ -\omega^2(m_{ij} + A_{ij}) - \mathrm{i}\omega B_{ij} + C_{ij}\Big\} = F_i^D \tag{49}$$

for $i = 1, 2, \cdots, 6$ and with m_{ij} the inertial matrix, and (A_{ij}, B_{ij}, C_{ij}) defined in (47).

6. NUMERICAL IMPLEMENTATION

The numerical method implemented in [18] was associated with the boundary condition (6) on

F of Neumann-Kelvin type and the boundary condition (7) on H including the ship-shaped stream. The ship hull is represented by a number of bi-quadratic curved patches of 9 nodes. Not only a precise description of ship geometry is achieved, but also a continuous representation of the velocity potential over the hull can be obtained so that the tangent derivatives can be computed by making differentiation to the shape functions as described in [18].

The new BIE (33)-(35) associated with the boundary condition on F and based on the ship-shaped stream gives the velocity potential $\varphi(P)$ on H and F. Its derivatives are necessary for computing wave loads and induced motions. The bi-quadratic patch method developed in [18] is then preferred. In order to take advantages of analytical integrations of Green's function on panels represented by formulae (22) and (26), the subdivision of curved patch into flat panels is performed as a pre-build-in treatment. The new BIE is then written at centroids of flat panels. The domain collocation of Galerkin type is then adopted by an integration of both sides of BIE over the field panel. P2P formulations (26) play then a critical role here for obtaining accurate influence coefficients to fill the matrix of linear system. Once the BIE is solved, the solution (velocity potential) on flat panels inside of one patch is then mapped to that at patch's nodes. The potential and its derivatives can then be re-computed at any point on the curved patch by using shape functions and potential values at patch's nodes.

6.1. Bi-quadratic patch and flat panels

The bi-quadratic patch described in [18] is subdivided into 9 (3×3) quadrilateral flat panels as shown on the left of Figure 7. The pane's centroid and its 4 corner nodes are located on the curved patch with some tolerance of warpness. Subdivision of a quadratic patch with 7 nodes into 6 triangular flat panels or 6 quadrilateral plus one hexagonal panels can also be made in similar ways.

An example of mesh containing geometrical information of both bi-quadratic patches and flat panels is illustrated in the middle picture of the same Figure 7. The hullform is that of Wigley IV presented in [23]. Red lines represent the border contour of curved patches and black lines indicate the border sides of quadrilateral flat panels. On the waterplane W inside the hull H, the quadrilateral flat panels are automatically generated according to the geometrical data of curves patches which touch the waterline, with a requirement of panel size to be comparable with that of panels on H. The grid on W is a bit arbitrary and no need to fill the whole waterplane.

On the right part of Figure 7, the grid on the free surface F is illustrated. Again, patch's border contours are shown by red lines and panel's borders by black lines. The flat patch (and flat panels) in the vicinity of hull must be finer due to the fact that the ship-shaped flow varies rapidly near the waterline. The layers of patches on F are of ellipse form to be better married to the waterline. By using elliptic coordinate parameters, the border contours of patches cross each other at the orthogonal angle, except those touching the waterline in the nearest layer of patches.

6.2. Integrals on the free surface

The numerical method based on Neumann-Kelvin boundary condition (6) on F developed in [18] has been validated with analytical results at zero speed for a floating hemisphere, semi-analytical solutions of NK steady flow around an ellipsoid and semi-analytical results for a submerged sphere advancing in waves. The comparison with experimental measurements performed in [23] has been fairly good for the Wigley hullform III which is a very slender body with length/width ratio = 10 (typical commercial ship has a ratio about 6 to 8). Nevertheless, the comparison for the Wigley hullform IV (with the length/width ratio = 5) was fairly bad, in particular, hydrodynamic coefficients (added-mass and damping) in pitch are very sensitive to the parameters like filter constant designed to remove highly oscillations in Green's function computation and number of Gauss points for integration of Green's function over patches.

Now we have new set of boundary integral equations not only on the ship hull H (33), but also over a zone on F (34) in the vicinity of ship, and additional zero-potential requirement imposing on the waterplane W (35) inside the hull. To examine the effect of integral on F, we have simplified it by taking the dominant terms

$$\iint_F (F_0\varphi + F_1\varphi_x + F_2\varphi_y)\,\mathrm{d}S$$
$$\approx \iint_F \left[\bar{\phi}_x(G_z - \omega^2 G) + 2\mathrm{i}\tau\bar{\phi}_y G_y - \mathrm{i}\tau\bar{\phi}_{zz}G\right]\varphi\,\mathrm{d}S \tag{50}$$

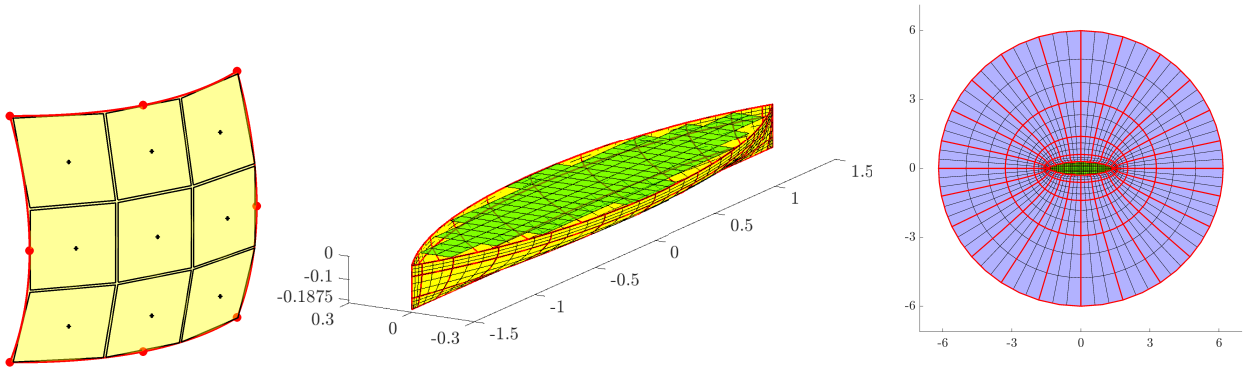

Figure 7. Subdivision of quadratic patch into flat panels (left), the mesh composed of patches and panels on H and W (middle) and the mesh on F (right).

and all terms of $O(F_{\rm r}^2)$ are ignored in the present computations. The variations of $(\bar{\phi}_x, \bar{\phi}_y, \bar{\phi}_{zz})$ involved in the forcing terms of above integral are depicted on the left, in the middle and on the right of Figure 8, respectively. They are significant at bow and stern as expected and decay very rapidly with distance from bow or stern, in consistence with the theoretical order: $\nabla\bar{\phi} \approx O(R^{-3})$ and $\nabla(\nabla\bar{\phi}) \approx O(R^{-4})$ with R the distance from ship center, for large R. The zone presented in Figure 8 around the Wigley hullform IV, has a total distance of $2L$ (two times the ship length)) extending along the ship centerline.

6.3. Radiation coefficients

The same Wigley hullform IV, described in [23], with length L=3m, width B=0.6m and draft D = 0.1875m is considered. The hull surface is discretized with 72 bi-quadratic patches illustrated in the middle of Figure 7. The hull patches are then subdivided into 648 (9×72) flat panels. There are 148 flat panels placed on the waterplane W inside the hull. The free surface F in a zone of diameter about $4L$ around the ship is meshed with 96 patches (864 panels) as well. Numerical results and comparison with experimental measurements in [23] are presented on the four lines of Figures 9, respectively, for hydrodynamic coefficients in heave, pitch, heave-pitch and pitch-heave coupling oscillations. The added-mass coefficients and damping coefficients are illustrated on the left and right pictures, respectively. The case with Froude number $F_{\rm r} = U/\sqrt{gL} = 0.3$ is taken for all results here. The abscissa in all pictures in Figures 9 are reduced encounter frequency $\omega\sqrt{L/g}$. The added-mass coefficients A_{33}, A_{55} and $A_{35}(A_{53})$ are non-dimensionalized respectively by (ρV), $(\rho V L^2)$ and $(\rho V L)$ with the displacement $V = 0.156\text{m}^3$. The damping coefficients B_{33}, B_{55} and $B_{35}(B_{53})$ are divided respectively by $(\rho V\sqrt{g/L})$, $(\rho V L^2\sqrt{g/L})$ and $(\rho V L\sqrt{g/L})$. The results of model tests provided in [23] are represented by squares and filled triangles for two series of measurements.

In all pictures, there are three series of numerical results including those based on the so-called "encounter-frequency" approximation implemented in HydroStar (Original version of zero speed) with legend (HydroStar-O) and by dashed lines, those by using classical boundary integral equations (Classical NK) of Neumann-Kelvin type (31) developed in [18] depicted by blue lines, and the results obtained by the present method represented by "HydroStar-V" and depicted by red lines. The encounter approximation (dashed lines) yields correct results at very high frequencies but totally wrong in the zone of low frequencies. The Classical NK (blue lines) gives fairly good results for added-mass in heave (A_{33}), still correct for damping in heave (B_{33}) with some more deviations at larger frequencies. Concerning hydrodynamic coefficients in pitch, the differences between numerical results and benchmark measurements are increased for added-mass (A_{55}) and largely enhanced for damping (B_{55}). As mentioned, the waterline integrals involved in the Classical NK are very sensitive to the parameters introduced in the numerical implementation. The results presented here are one of best series, i.e., other results could present even more important oscillations. If we consider the middle of oscillations, the results could be more or less consistent with the benchmark results for added-mass coefficients, but not for damping coefficients. In particular, the damping coefficients

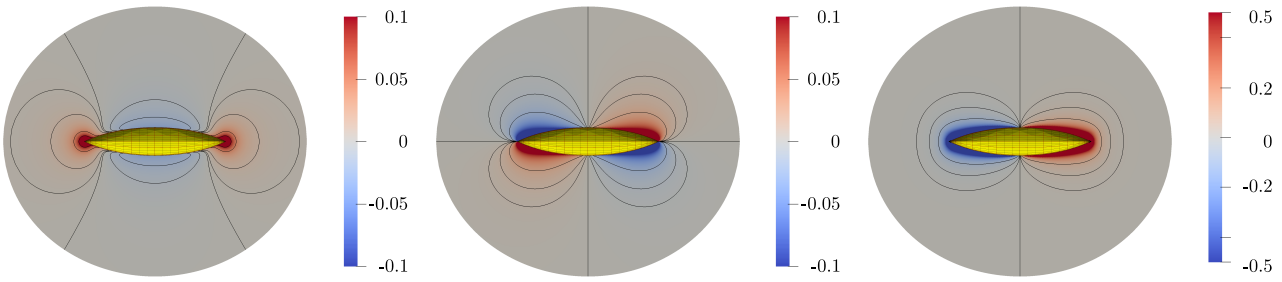

Figure 8. Forcing terms on F due to ship-shaped stream: $\bar{\phi}_x$ (left), $\bar{\phi}_y$ (middle) and $\bar{\phi}_{zz}$ (right)

B_{55} obtained by the Classical NK oscillate with amplified magnitude. The middle of oscillations deviates largely from benchmark "level". On the last two lines of Figures 9, the heave-pitch coupling coefficients (A_{35}, B_{35}) and (A_{53}, B_{53}) are depicted. Again, oscillations in both added-mass and damping coefficients are remarkable.

The results by the New BIE (HydroStar-V) represented by (33)-(35) are depicted by the red lines marked with circles for added-mass and damping coefficients. The curves of results are smooth and free of "irregular" oscillations present in those by the Classical NK. Furthermore, the results of HydroStar-V are in very good agreement with benchmark measurements. In particular, the added-mass coefficients (A_{33}, A_{55}) obtained by using (47) including the speed-effect stiffness, are in excellent agreement with the measurements. Some slight difference for other quantities could be explained by "normal" numerical errors. Concerning the heave-pitch coupling coefficients, added-mass coefficients by HydroStar-V are in very good agreement with experimental measurements. The results of damping coefficients are smooth and follow well the benchmark results, unlike those by Classical NK presenting oscillations. It worth noting that there is not any parameters implemented in the method except the value of viscosity to be given. Although the value of $\epsilon = 0.0001$ is advocated, using smaller values does not affect the final results, but increases intermediate computations.

6.4. Diffraction loads and induced motions

The diffraction loads defined by (48) are computed and illustrated on Figure 10. The amplitudes of the forces in heave F_3 are scaled by $(H_{33}a)$ using the hydrostatic stiffness H_{33} and wave amplitude a following that in [23], and depicted on the left of Figure 10. The amplitudes of the moments in pitch F_5 are scaled by $(H_{55}k_0a)$ using the hydrostatic stiffness H_{55} and wave steepness (k_0a) of incoming waves, and depicted on the right of Figure 10. Globally, all three series of results are quite similar and close to the measurements. The classical NK method provides fairly good results. The results obtained by using the new BIE (HydroStar-V) are much better than those of classical NK and in very good agreement with the measurements of model tests given in [23], in particular, in the zone of reduced encounter frequencies $\omega\sqrt{L/g} \in (2.5, 5.0)$ for both in heave and pitch.

Finally, the motion RAOs of heave and pitch are shown on Figure 11. The heave RAO illustrated on the left is scaled with the incoming wave amplitude a. The pitch depicted on the right is scaled with the wave steepness (k_0a) of incoming waves. At low wave frequencies, both RAOs tend to unity in accordance with physical observations. For the heave RAO, all three methods predict well the resonance frequency $(\omega_3\sqrt{L/g} \approx 3.5)$ at which the response is maximum. However, both the "encounter frequency" approximation (HydroStar-O) and the classical NK method predict larger resonant motions in heave. The results by the "encounter frequency" approximation exaggerate much the response in large range of frequencies on both sides of the resonance. The results by the new BIE (HydroStar-V) are in very good agreement with the measurements in [23], in the full range of frequencies.

Concerning the pitch RAO, both the "encounter frequency" approximation and the classical NK method provide the results deviated from the measurements of model tests in [23]. The peak position is confusing and lower than the benchmark. Even two peaks are visible in the results by the classical NK method due to the "irregular" oscillations of added mass (and damping) coefficients shown on Figure 9. On the other side, the results obtained by the new BIE (HydroStar-V) are in excellent agreement with the measurements given in [23].

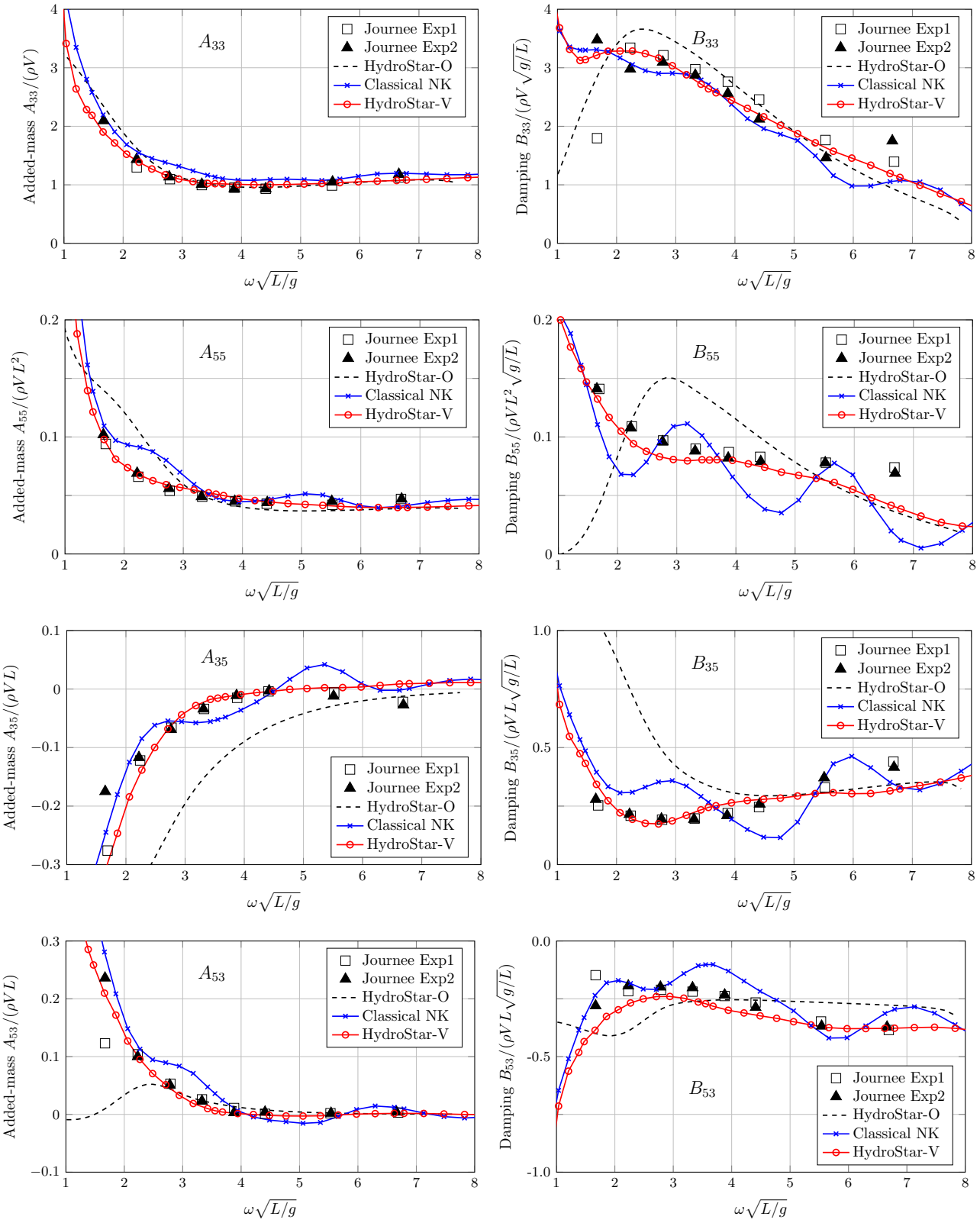

Figure 9. Added-mass coefficients (left) and damping coefficient (right) in heave (first line), pitch (second line), heave-pitch (third) and pitch-heave (fourth line) coupling oscillations

7. DISCUSSION AND CONCLUSION

We have presented our most recent results of research work on the free-surface Green's function method (GFM) applying to the ship seakeeping with forward speed. Most of them are unpublished and only a summary presented very re-

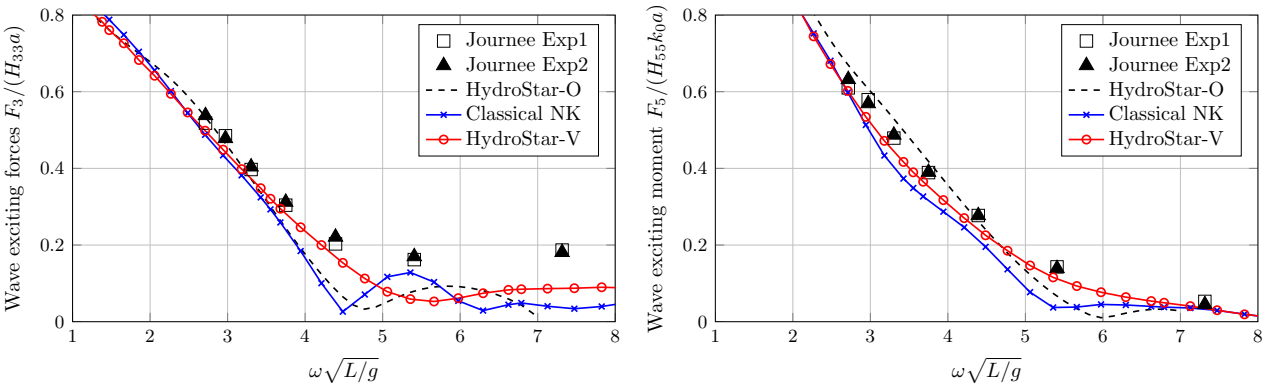

Figure 10. Diffraction wave loads in heave (left) and in pitch (right)

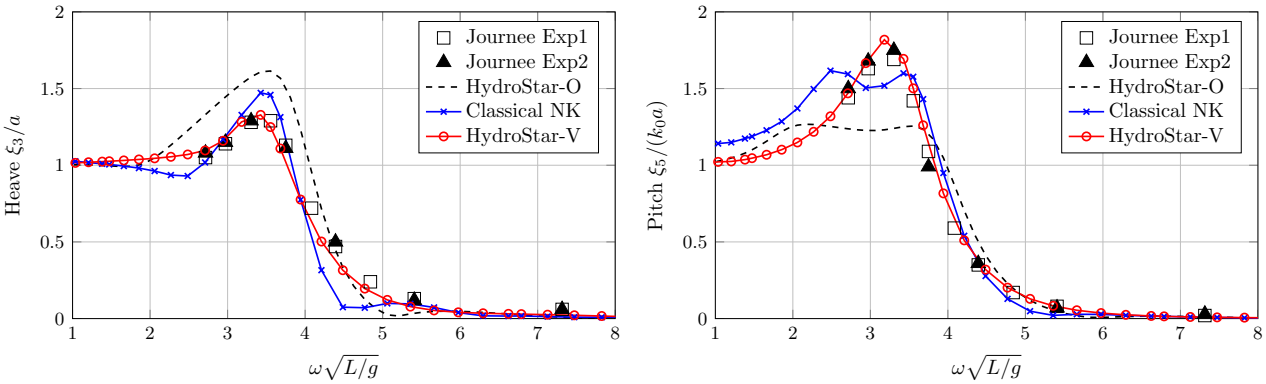

Figure 11. Heave RAO (left) and Pith RAO (right)

cently in [26]. Indeed, facing the complexity of the subject, we have raised the challenge by laying down the critical cornerstones.

On top of all, we have re-analysed the boundary value problem by choosing the ship-shaped stream as the base flow. This consideration is not only for physical acceptance but also necessary by a rigorous analysis based on the perturbation theory. The new and consistent boundary condition on the free surface is obtained with linearisation over the base flow. Unlike the usual boundary condition (6) of Neumann-Kelvin type based on the uniform flow (physically unacceptable), the formulation (5) looks more complex due to the interaction terms associated with the base flow.

We find the benefit of this complex boundary condition in the formulation of boundary integration equations. Green's theorem is applied to Green's function and velocity potential of unsteady flow by performing the vector integral analysis of their respective differential equations. The part of free-surface integrand corresponding to the terms associated with the uniform flow is modified such that the equivalent waterline integral is proportional to the normal derivative of the base flow. This waterline integral is then simply nil by the boundary condition of base flow on ship hull. Free of waterline integral, it remains still integration of some free surface terms. This remaining integral over the free surface is localized in a limited zone as the integrand function depending on the ship-shaped stream is significant only in the vicinity of hull.

Green's function associated with a pulsating and translating source represents the fundamental solution to ship-motion problems with forward speed. Many studies have been carried out to analyse its behaviours and to develop numerical schemes for its computations. The most striking property is the peculiar singularity and fast oscillations for field points approaching to the track of source point at or close to the free surface, as revealed in [15]. This behaviour makes the waterline integral included in the Old BIE (Classical NK) nightmarish. The same issue should be encountered in the computation of the free-surface integral involved in the New BIE.

Not satisfied with using treatments by lower-

ing the waterline or by parametrising numerical filters to mask the difficulty, we have examined its origin by introducing the neglected physical parameters like surface tension, fluid viscosity or combination of both. We have chosen here the introduction of viscosity. Unlike the classical way introducing fictitious viscosity (Rayleigh viscosity or Lighthill's argument) which was just a mathematical device to make waves propagating radially outwards, the analysis based on linearised Navier-Stokes equation and Helmholtz decomposition in [16] yields the consistent kinematic and dynamic boundary conditions on the free surface with viscosity.

Green's function with viscosity is then adopted. Unlike the inviscid Green's function, there are three complex wavenumbers. First two resemble those of inviscid Green's function for small and moderate values, but significantly different for θ close to $\pi/2$. They can be large but not unbounded and have an important imaginary part which damps all highly oscillatory waves. The third one having a negative real part does not generate any waves and contribute to the local field. Being implicit and complex, the integrand function of viscous Green's function is free of singularities and numerical computations are facilitated.

As the matrix elements of linear system, the influence coefficients are the integration of Green's function and its derivatives on ship hull H and on free surface F. To guarantee the accuracy, analytical integrations of the wavenumber integral function and its derivatives over flat panels of polygonal form are formulated for all configurations including panels of hull-to-hull, hull-to-freesurface and freesurface-to-freesurface. The usual algorithm using Gauss points gives good accuracy for integration on hull panels. It is, however, nearly impossible, or to have to use excessive number of Gauss points up to (256×256) to obtain a correct accuracy for panels on the free-surface.

To take advantages associated with the accuracy in the analytical integrations of Green's function over flat panels, we adopt the concept to use flat panels inside a bi-quadratic curved patch represented by using shape functions. The velocity potential obtained by New BIE (HydroStar-V) on flat panels can be accurately extended to its tangent derivatives necessary for pressure computations, by the derivatives of the shape functions.

The last but not the least. To be sure that Green's theorem is well respected outside the fluid domain, the zero potential on the waterplane inside the ship hull is imposed in additional to BIEs on the hull and on the free surface. This over-determined linear system method, described in [24], has been successful to remove the effect of "irregular frequencies", in our in-house software HydroStar-O for the solution of seakeeping at zero speed. Application of this approach guarantees the well-condition of linear system. Indeed, there is an issue of "irregular wavenumebrs" associated with BIEs in the forward-speed problem. Similar to the zero-speed case which is a special case of forward-speed problems, the effect of "irregular wavenumbers" appears for every encounter frequency, remarkable in Figures 9 by the exaggerated oscillations of hydrodynamic basic solutions, in particular, the damping coefficients obtained by using the Classical NK method.

In summary, the new method presented here accumulates a series of critical groundwork on both theoretical and numerical aspects. Based on sound theoretical advances and rigorous numerical developments, the results show convincing convergence and very good agreement with benchmark results derived from the classical experimental measurements. We have achieved our objective to have a reliable and practical tool to predict the seakeeping of a ship advancing in waves.

8. REFERENCES

[1] G. Fernandez & A. Jami (1987) La tenue à la mer des navires élancés: est-t-elle une affaire d'échelles multiples? *Actes des 1èmes J. de l'Hydrodynamique*, Nantes.

[2] F. Noblesse, D. Hendrix & A. Barnell (1989) L'approximation du navire élancé: Comparaison de mesures expériemntales et de prédictions numériques. *Actes des 2èmes J. de l'Hydrodynamique*, Nantes.

[3] J. Bougis & T. Coudray (1991) Méthodes rapides de calcul des fonctions de Green des problèmes de Neumann-Kelvin et de diffraction-radiation avec vitesse d'avance. *Actes des 3èmes J. de l'Hydrodynamique*, Grenoble.

[4] J.F. Le Guen, A. Magee & C. Royal (1993) Validation mutuelle de différents codes de tenue à la mer. *Actes des 4èmes J. de l'Hydrodynamique*, Val de Reuil.

[5] X.B. Chen, F. Noblesse & C. Yang (1995) Méthode de Fourier-Kochin-Lighthill pour la diffraction-radiation par un navire ou une structure offshore. *Actes des 5èmes J. de l'Hydrodynamique*, Rouen.

[6] A. Brument & G. Delhommeau (1997) Evaluation numérique de la fonction de Green de la tenue à la mer avec vitesse d'avance. *Actes des 6èmes J. de l'Hydrodynamique*, Nantes.

[7] J.P. Boin, M. Guilbaud & M. Ba (1999) Précision des intégrations surfaciques de la fonction de Green dans un code de tenue à la mer avec vitesse d'avance. *Actes des 7èmes J. de l'Hydrodynamique*, Marseilles.

[8] M. Ba, J.P. Boin, G. Delhommeau, M. Guilbaud & C. Maury (2001) Seakeeping computations using the diffraction-radiation Green's function with forward speed. *Actes des 8èmes J. de l'Hydrodynamique*, Nantes.

[9] L. Diebold & X.B. Chen (2001) Solution semi-analytique du problème de l'écoulement autour d'une semi-sphère avançant sur la surface libre. *Actes des 8èmes J. de l'Hydrodynamique*, Nantes.

[10] X.B. Chen, M. Guilbaud, L. Diebold & Y. Doutreleau (2003) Méthode de panneaux quadratiques pour la résolution du problème de la tenue à la mer avec vitesse d'avance: Comparaison avec l'approximation de fréquence de rencontre. *Actes des 9èmes J. de l'Hydrodynamique*, Poitiers.

[11] F. Noblesse (2005) Generalized boundary-integral representations of 3D flow about a ship advancing in regular waves. *Actes des 10èmes J. de l'Hydrodynamique*, Nantes.

[12] I. Ten & X.B. Chen (2010) Combined Rankine and Kelvin singularity method for seakeeping of an advancing ship with forward speed in waves. *Actes des 12èmes J. de l'Hydrodynamique*, Nantes.

[13] X.B. Chen, H. Liang, R.P. Li & X. Feng (2018) Ship seakeeping hydrodynamics by multi-domain method. *Proc. 32nd Symp Naval Hydrodynamics*, Hamburg (Germany).

[14] J.N. Newman (1991) The quest for a three-dimensional theory of ship-wave interactions. *Pil. Trans. Royal Soc. A* 334 (1634), 213-27.

[15] X.B. Chen & G.X. Wu (2001) On singular and highly oscillatory properties of the Green function for ship motions. *J. Fluid Mech.*, 445 (1), 77-91.

[16] X.B. Chen, F. Dias & W.Y. Duan (2011) Introduction of dissipation in potential flows. *Proc. 7th Intl Workshop on Ship Hydro*, Shanghai (China), 1-10.

[17] R. Brard (1972) The representation of a given ship form by singularity distributions when the boundary condition on the free surface is linearized. *J. Ship Res*, 16, 79-92.

[18] X.B. Chen, L. Diebold & Y. Doutreleau (2001) New Green-function method to predict wave-induced ship motions and loads. *Proc. 23rd Symp. Naval Hydro.*, Val de Reuil, 66-81.

[19] X.B. Chen (2020) Notes on ship-motion problems: Green's function and boundary integral equations. *Technique report*, Bureau Veritas, Paris.

[20] M. Abramowitz & I.A. Stegun (1967) Handbook of mathematical functions. *Dover Publications.*

[21] P. Guével (1980) L'écoulement à surface libre: Préliminaires mathématiques. E.N.S.M. Nantes.

[22] F. Noblesse (1983) Integral identities of potential theory of radiation and diffraction of regular water waves by a body. *J. Eng. Math.*, 17, 1–13.

[23] J.M.J. Journée (1992) Experiments and claculations on four Wigley hullforms. *Delft Univ. Techn. Ship Hydromechanics Lab.* Report No.909.

[24] H. Liang, C. Ouled Housseine, X.B. Chen & Y.L. Shao (2020) Efficient methods free of irregular frequencies in wave and solid/porous structure interactions. *J. Fluids and Structures*, 98, 1-16.

[25] M. Kashiwagi (1994) A new Green-function method for the 3-d unsteady problem of a ship with forward speed, *Proc. 9th IWWWFB*, Kuju (Japan).

[26] X.B. Chen, Y.M. Choi, S. Malenica & Q. Derbanne (2020) Ecoulement instationnaire sur le courant dévié par le navire - Solution pour la tenue à la mer avec vitesse d'avance. *Actes des 17èmes J. de l'Hydrodynamique*, Cherbourg-en-Cotentin.